Product quantum-state-dependent anisotropies in photoinitiated unimolecular decomposition

A. V. Demyanenko, V. Dribinski, and H. Reisler[a)]
Department of Chemistry, University of Southern California, Los Angeles, California 90089-0482

H. Meyer
Department of Physics and Astronomy, University of Georgia, Athens, Georgia 30602-2451

C. X. W. Qian
Department of Chemistry, University of Victoria, P.O. Box 3065, Victoria, British Columbia, Canada V8W 3V6

(Received 8 June 1999; accepted 22 July 1999)

Angular distributions of state-selected NO and O products in the photoinitiated unimolecular decomposition of jet-cooled NO_2 have been measured by using both the photofragment ion imaging technique with velocity map imaging and ion time-of-flight translational spectroscopy. The recoil anisotropy parameter of the photofragments, β, depends strongly on the rotational angular momentum of the photoproduct. $O(^3P_{j=2,0})$ angular distributions are recorded at photolysis wavelengths 371.7, 354.7, and 338.9 nm. At these wavelengths, respectively, vibrational levels $v=0$, $v=0,1$ and $v=0-2$ of NO are generated. In addition, β values for $NO(v=2)$ in specific high rotational levels are determined at ~338 nm. The experimental observations are rationalized with a classical model that takes into account the transverse recoil component mandated by angular momentum conservation. The model is general and applicable in cases where fragment angular momentum is large, i.e., a classical treatment is justified. It is applied here both to the experimental NO_2 results, and results of quantum calculations of the vibrational predissociation of the Ne–ICl van der Waals complex. It is concluded that deviations from the limiting β values should be prominent in fast, barrierless unimolecular decomposition, and in certain dissociation processes where a large fraction of the available energy is deposited in rotational excitation of the diatom. The application of the model to NO_2 dissociation suggests that the nuclear dynamics leading to dissociation involves a decrease in bending angle at short internuclear separations followed by a stretching motion. This interpretation is in accord with recent theoretical calculations. [S0021-9606(99)00239-1]

I. INTRODUCTION

Measurements of product angular distributions in photodissociation dynamics can provide detailed information on the symmetry of the dissociative electronic transition, the subsequent dynamics of product evolution, and the time scale of the dissociation.[1] Since the pioneering work of Zare and Herschbach,[2(a)] these measurements have become a versatile, albeit complex, tool in the arsenal of experimental techniques of chemical physics. The angular distributions reflect several well-known vector correlations, among which the most common is the correlation between the electronic transition dipole moment $\boldsymbol{\mu}_{\boldsymbol{\varepsilon}}$ and the fragment recoil velocity $\mathbf{v}$ ($\langle \boldsymbol{\mu}_{\boldsymbol{\varepsilon}} \cdot \mathbf{V} \rangle$). The $\langle \boldsymbol{\mu}_{\boldsymbol{\varepsilon}} \cdot \mathbf{V} \rangle$ correlation is characterized in terms of the recoil anisotropy parameter, β, and is determined in the space fixed frame (SFF) of coordinates. The product angular distribution is described by the standard recoil anisotropy function,[1,2]

$$P(\theta) = \frac{1}{4\pi}[1 + \beta \cdot P_2(\cos\theta)], \tag{1}$$

where θ is the angle between the recoil velocity vector and the laser polarization vector $\mathbf{E}$, and $P_2(x)$ is the second Legendre polynomial. In the limit of fast dissociation and axial recoil, $\beta = 2$ and -1 are obtained when the transition dipole moment is parallel or perpendicular, respectively, to the fragment velocity vector. Both classical and quantum mechanical models have been developed to describe β.[1–6]

In most of the systems for which β has been measured, photofragmentation has been accompanied by significant translational energy release. The work described here is different in that the fragments possess high internal excitation accompanied by small kinetic energy release, a situation characteristic of unimolecular decomposition. We report studies of the photoinitiated unimolecular decomposition of NO_2 which demonstrate that as a result of a significant transverse recoil component, β depends sensitively on the rotational state of the NO fragment, and to a lesser degree on NO vibration. The larger the rotational excitation, the larger the transverse recoil component that accompanies the fragmentation.

It is well established both experimentally and theoretically that molecular rotation prior to dissociation can affect the observed value of β.[7,8] It has also been pointed out that parent vibrational motion prior to, and nuclear motions during the dissociation can influence β under conditions which

a)Electronic mail: reisler@chem1.usc.edu

are related to the specific dissociation dynamics.[9]

Product state-dependent β in photodissociation has been reported before. For example, Mordaunt *et al.* developed a pseudotriatomic model for the 193-nm photodissociation of NH_3 that explained the observed changes in β as a function of the N quantum number of NH_2.[10] Their classical model, based on angular momentum conservation and impulsive dissociation, assumed that dissociation commenced at the point of the conical intersection, and involved out-of-plane torques. Kable *et al.* used a model involving Renner–Teller interaction to interpret the observed β changes in the photodissociation of HCO.[11] Beswick and co-workers, in a quantum mechanical calculation of the photoinitiated predissociation of Ne–ICl and Ne–Cl_2 complexes, demonstrated a substantial change of β as a function of the rotational quantum number of the diatomic fragment.[4] In a classical trajectory calculation, Loock *et al.* predicted that a triatomic parent bending motion will influence the fragment angular distribution in a way that depends on the rotational state of the diatomic fragment.[9] A dependence of β on fragment speed was observed in ozone photodissociation, and on N_2 rotational state—in N_2O photodissociation.[12] The dependence of β on the NH rotational level in HN_3 photolysis has been interpreted as resulting from out-of-plane motions during the dissociation.[13]

The photoinitiated unimolecular decomposition of NO_2 has been investigated extensively, and serves as a benchmark for statistical models of unimolecular reactions.[14] This paper is concerned with the angular distributions of the photofragments and their dependence on the fragment quantum state, and a model is proposed to explain the observed dependencies. Dissociation takes place predominantly on the ground potential energy surface (PES), following excitation to the mixed $1\,^2B_2/1\,^2A_1$ state via a parallel transition. Strong vibronic coupling between the states results from a conical intersection located near the bottom of the $^2B_2$ state.[14–16] The dissociation rate of jet-cooled NO_2 is fast, and the products exhibit spatial anisotropy.[17,18] The NO state distributions, despite severe fluctuations, can be described on average using statistical theories, implying dissociation on a barrierless PES.[14,19,20] Rate measurements[21,22] and theoretical calculations[15,16,23,24] have led to the same conclusion.

Fragment angular distributions in NO_2 photodissociation were determined first by Busch and Wilson, who used 370-K samples and 347-nm photolysis.[18] Their results of the average value of β were confirmed by other investigators.[25,26] Subsequent studies with jet-cooled samples (<5 K) demonstrated the effect of parent rotation on decreasing the magnitude of β, and concluded that the dissociation rate of jet-cooled NO_2 is faster than the characteristic time of parent rotation.[17]

A puzzling dependence of β on the fragment rotational state was first reported by Butenhoff and Rohlfing,[27] who found that near dissociation threshold ($D_0 = 25\,130\ \mathrm{cm}^{-1}$), the highest NO rotational levels exhibited markedly diminished anisotropy. More recently, Liu and co-workers reported time-of-flight (TOF) studies of the $O(^3P_{j=2,1,0})$ photofragments at 355 nm that showed a gradual decrease in β with decreasing total center of mass (c.m.) translational energy, E_t.[28] In addition, an effect due to the spin-orbit state was observed: the angular distribution of the highest spin-orbit state, $^3P_0$, was characterized by a lower β at all translational energies, compared to the other spin-orbit states. The energies of the spin-orbit states are: $^3P_2:{}^3P_1:{}^3P_0 = 0:158:226\ \mathrm{cm}^{-1}$. Huber and co-workers, who carried out TOF measurements of oxygen (without state selection) at 355 and 351 nm, also obtained E_t-dependent β parameters.[29] To date, no model has been offered to explain these observations.

In this paper, we report studies of $O(^3P_{j=2,0})$ angular anisotropy as a function of fragment recoil velocity carried out at photolysis wavelengths 371.7, 354.7, and 338.9 nm. These wavelengths correspond to energies in excess of D_0 of 1776, 3065, and 4380 cm^{-1} where, respectively, $v=0$, $v=0,1$, and $v=0-2$ vibrational levels of NO are open. In addition, β values for $NO(v=2)$ associated with high rotational levels J (low E_t) were determined at $\sim$338 nm.

The experimental observations are rationalized with a classical model that takes into account (i) transverse recoil; (ii) the evolving nuclear dynamics. The model is general and applicable in cases where fragment angular momentum is large (i.e., a classical treatment is justified), but can also be related to the quantum mechanical treatment. It is applied here both to the experimental NO_2 results, and to results of quantum calculations on the vibrational predissociation of the Ne–ICl van der Waals complex. We note that in contrast to direct photodissociation, where product state distributions provide clear signatures of exit-channel dynamics, the statistical NO state distributions in NO_2 decomposition are not sensitive to the shape of the PES. A dependence of β on the internal energy of the diatomic product can then serve as a useful probe of the dynamics.

The paper is organized as follows. The experimental observations of the fragment angular distributions in NO_2 dissociation are described first. Two techniques are used: photofragment ion imaging and ion TOF translational spectroscopy. A simple model based on conservation laws is then presented, which gives a physical interpretation of the experimental observations. This model is also applied to the vibrational predissociation of the Ne–ICl complex, and β vs J_{ICl} is compared to the corresponding results obtained by quantum mechanical calculations.[4] We end this paper with a discussion of the implications of the β variation to NO_2 dissociation mechanism, and an evaluation of other dissociative systems where a similar β variation is expected.

II. EXPERIMENTAL METHODS

A. Experimental arrangement

The experiments at the University of Georgia and the University of Southern California (USC) both use molecular beams of NO_2 seeded in either Ne or He/Ne, and resonance enhanced multiphoton ionization (REMPI) for product detection. NO is detected in a one-color experiment, while O atoms are detected in experiments where the pump and probe frequencies are different.

Details of the Georgia apparatus have been described

previously.[30] Briefly, the NO_2 beam is generated by expanding a mixture of 4% NO_2 in Ne through a piezoelectric molecular beam source (60-μs duration, 10 Hz) at a backing pressure of 1.8 atm. The gas pulses pass through a skimmer into the scattering chamber where they are intersected at right angle by the photolysis/probe laser. The interaction with the laser pulse takes place in an electric drift-field arrangement. Product ions are accelerated (10 V/cm) toward a microchannel plate (MCP) detector mounted off-axis. The velocity component of the neutral fragments is determined from the arrival time of the ions at the detector. The laser system is a Nd:YAG pumped dye laser (DCM dye), whose frequency near 680 nm is doubled in a KDP crystal. The resulting ultraviolet (UV) output ($\sim$0.6 mJ) is focused with a lens ($f=500$ mm) onto the molecular beam.

The ion-imaging arrangement has been described in detail elsewhere.[31] In brief, it consists of an ion-acceleration stage, a 60-cm-long drift tube, and a charge coupled device (CCD) camera that monitors a phosphor screen coupled to a MCP ion detector. The ion optics of the ion-acceleration stage is based on a scheme proposed by Parker *et al.* for velocity map imaging,[32] and consists of a repeller, an open extractor electrode (50-mm hole), and an open ground electrode (25-mm hole). At an optimal voltage ratio for the repeller and extractor plates, all ions with the same initial velocity are focused onto the same spot on the MCP detector.

A doubly skimmed pulsed molecular beam containing 3% NO_2 and 5% O_2 seeded in 1.8 atm of a He(30%)/Ne(70%) mixture propagates through a hole in the repeller plate. The NO_2 mixture is prepared by passing the carrier gas mixture over NO_2 kept at $-29\,^{\circ}$C (o-xylene slush). Further downstream, NO_2 ($T_{rot}\leqslant 2$ K) is photolyzed with pulsed, linearly polarized, and focused ($f=250$ mm) laser radiation (0.6–1.6 mJ) intersecting the molecular beam at right angle. Photolysis at 338–372 nm is achieved by using the frequency-doubled output of a Nd:YAG laser pumped dye laser system. The polarization of the photolysis light is directed perpendicular to the molecular beam, in a plane parallel to the detector plane.

In the two-color ion-imaging experiments, the output of an excimer-laser pumped dye laser system (Coumarin 450) is frequency doubled to probe the $O(^3P_j, j=0,2)$ fragments by $2+1$ REMPI via the $3p\,^3P \leftarrow 2p\,^3P$ transitions at 225.68 and 226.28 nm, respectively. Due to the Doppler width of the $O(^3P_j)$ fragments, the probe frequency is scanned over the entire bandwidth to ensure that the images include all product velocities. The dissociation and probe lasers are both linearly polarized, and introduced coaxially at right angle to the molecular beam. To minimize complications due to vector correlations, the polarizations of the two lasers are fixed parallel to each other. The time delay between the pump and probe lasers is kept at $\tau_d=0\pm 5$ ns. Typical signals include summation of $1-2\times 10^4$ laser firings.

Experimental complications in the two-color experiments arise from dissociation by the probe radiation, and photolysis of residual gases. To eliminate this contamination, a subtraction routine is employed, which takes into account two types of background signals: (i) signal obtained with the pump and probe lasers on, but delayed with respect to the molecular beam accounts for ions generated from residual gases. (ii) Signal obtained at the temporal maximum of the molecular beam pulse, but with the pump laser off accounts for background generated by the probe alone. Both types of background give spatially isotropic signals. The second type of contamination is substantial only when $O(^3P_0)$, whose fractional population is low, is probed, since higher probe energies are required for its detection [0.2–0.4 mJ, as compared with 0.03–0.1 mJ for $O(^3P_2)$]. Good spatial and temporal overlap of the two laser beams minimizes effects due to the probe.

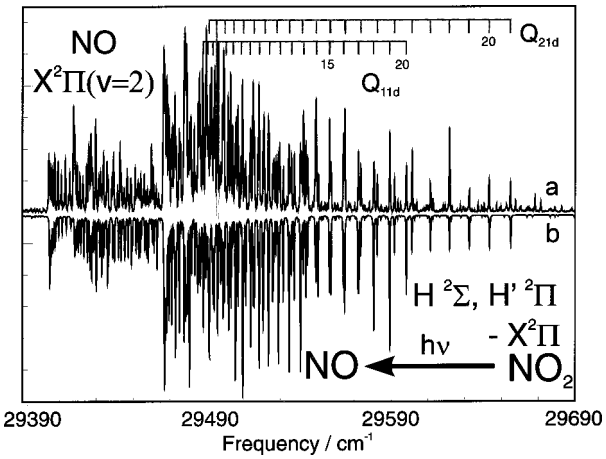

FIG. 1. $(2+1)$ REMPI spectrum of NO resulting from the photodissociation of NO_2 in the region of the $H\,^2\Sigma, H'\,^2\Pi(v'=0) \leftarrow X\,^2\Pi(v''=2)$ hot band transition (top trace). The bottom trace represents a simulation assuming a rotational temperature of 2000 K. See text for details.

B. Two-photon spectroscopy of the NO $H\,^2\Sigma, H'\,^2\Pi(v'=0) \leftarrow X\,^2\Pi(v''=2)$ transition

In the photolysis wavelength range around 340 nm, vibrationally excited NO $X\,^2\Pi(v=2)$ products are detected by $(2+1)$ REMPI via the $H\,^2\Sigma, H'\,^2\Pi(v'=0)$ state. The two-photon spectroscopy of this Rydberg state has been discussed in detail previously.[33] The one-color NO($v=2$) REMPI spectrum resulting from NO_2 photodissociation is shown in the top part of Fig. 1. The spectrum in the bottom part is calculated assuming a rotational temperature of 2000 K, truncated to exclude rotational states whose energies exceed the available energy. The positions of the various rotational lines in the Q_{11d} and Q_{21d} branches are displayed at the top, following the notation of Huber and Miescher.[34] The $X-H$ two-photon transition is dominated by a zeroth rank tensor which gives rise to rotational Q-branch structures. In previous work, a much smaller contribution due to a second-rank tensor component was also identified.[33] While in an isotropic ensemble this contribution can usually be neglected, a different situation arises for an ensemble of product molecules, which is characterized by an anisotropic distribution of the rotational angular momentum. In this case, the two-photon signal is sensitive to the quadrupole and hexadecapole moments of the m_j distribution.

When the angular distribution of the photofragments is resolved, Beswick *et al.* have shown that the state multipole moments of the rotational angular momentum distribution

must be considered functions of the recoil direction.[4,35] With linearly polarized photolysis light, the angular distributions of the fragments are uniquely characterized by the recoil angle Θ with respect to the pump laser polarization direction. In this case, it can be shown that the $(2+1)$ REMPI signal is a function of both the direction of the probe laser polarization and the recoil angle. The two-photon intensity for a particular rotational NO product state J will depend on the alignment moments $T_0^{(0)}, T_0^{(2)}$, and $T_0^{(4)}$, which in turn will be functions of Θ,

$$I = \frac{n(J)}{B^{(0)}} \left\{ T_0^{(0)}(\Theta) + \frac{B^{(2)}}{B^{(0)}} T_0^{(2)}(\Theta) P_2(\cos\delta) + \frac{B^{(4)}}{B^{(0)}} T_0^{(4)}(\Theta) P_4(\cos\delta) \right\}. \quad (2)$$

Here we have used the state multipole moments $T_0^{(Q)}$ as defined by Blum, [36] which are proportional to the more familiar state multipole moments $A_0^{(Q)}$ introduced by Greene and Zare.[37] The angle δ describes the direction of the probe laser polarization with respect to the photolysis laser polarization. For a one-color photodissociation experiment, we necessarily have $\delta = 0$. The coefficients $B^{(Q)}$ depend on the angular momenta involved in the two-photon detection step. For the Q branches of the $X-H$ transition, we find approximately $B^{(2)}/B^{(0)} = -0.3$ and $B^{(4)}/B^{(0)} = -0.04$, independent of J. As shown in the Appendix, the multipole moments $T_0^{(Q)}$ are expanded in a series of Legendre polynomials $P_\lambda(\cos\Theta)$ with coefficients $C_\lambda^{(Q)}$. In this notation, the anisotropy parameter β is described in terms of the coefficients $C_2^{(Q)}$.

In a one-color experiment, it is impossible to disentangle the contributions due to the different state multipole moments. Nevertheless, the sensitivity of our experimental data to the vector correlations can be estimated from the contributions of higher order Legendre polynomials to the measured angular distributions. Within experimental uncertainty, no such contributions are obvious. Although it is well known that the NO products are aligned rotationally, we must conclude that the data presented here are not seriously affected by rotational alignment.[38] Neglecting the small contribution due to the hexadecapole moment $T_0^{(4)}$, we find the effective anisotropy parameter β_{eff} to be

$$\beta_{\text{eff}} = \beta - 0.3 C_2^{(2)}, \quad (3)$$

independent of fragment rotational level. The importance of the coefficient $C_2^{(2)}$, which is associated with the quadrupole moment $T_0^{(2)}$ (see Appendix), can only be determined in an experiment where the photolysis and probe laser polarization directions are controlled independently. Applying the method of laser-induced grating spectroscopy (LIGS) to the NO($v=0$) product detection near D_0, Butenhoff and Rohlfing conclude that β_{eff} does not change significantly when the probe laser polarization is rotated by 90°;[27] thus, the coefficient $C_2^{(2)}$ must be negligible. We expect that the contamination of the anisotropy parameter due to the rotational alignment will be small in our case as well.

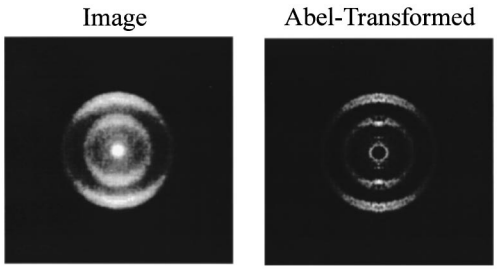

FIG. 2. Image of NO($^2\Pi_{1/2}, v=2, J=17.5$) and its Abel transform obtained via $(2+1)$ REMPI at 337.59 nm in a one-color experiment. The Abel transform represents a 2D cut (including the axis of cylindrical symmetry) through the 3D velocity distribution.

III. EXPERIMENTAL RESULTS AND ANALYSIS

The results obtained at USC and the University of Georgia are complementary in that the imaging experiments have their highest accuracy for products with the largest translational energy release, while in the Georgia experiments, the best accuracy is achieved when products' translational energy is low. In addition, in the USC experiments the angular distributions of the O($^3P_{j=2,1,0}$) products are obtained as well.

A. Photofragment ion imaging

Images were obtained for selected rotational levels of NO($v=2, J$) with ~338-nm photolysis, and for O($^3P_2$) and O($^3P_0$) fragments with 371.7-, 354.7-, and 338.9-nm photolysis. The electric field vector **E** of the photolysis laser is maintained parallel to the vertical direction of the image plane, and the product recoil velocities are aligned predominantly in the polar direction of the image. The images are symmetrized and, after background subtraction as described in Sec. II, are Abel-transformed using established procedures.[39]

Shown in Fig. 2 is the raw image, as well as a two-dimensional (2D) cut of the three-dimensional (3D) Abel-transformed image of NO($^2\Pi_{1/2}, v=2, J=17.5$) obtained with 337.59-nm photolysis in a one-color experiment. The three spin-orbit states of the correlated O fragment are clearly resolved. The ring correlated with O($^3P_0$) collapses to a spot at the center, since almost no translational energy is associated with this channel. Despite the brightness of this spot, the integrated intensity of the O($^3P_0$) channel is very small. Similar images were obtained for NO($v=2, J=14.5-20.5$).

While probing NO provides the angular distribution for each fragment in a well-defined quantum state, the oxygen-photofragment images allow an overview of the total NO rovibrational distribution correlated with each oxygen spin-orbit state, albeit with loss of state resolution, since at each E_t several NO(Ω, v, J) states can overlap. In Fig. 3, images of O($^3P_2$) and O($^3P_0$) obtained with 338.9-nm photolysis are shown. NO in $v=0,1,2$ is produced: the bright central spot corresponds to NO($v=2, J$), the intense inner ring marks the onset of NO($v=1, J$), while the faint outermost ring is associated with NO($v=0, J$). Similar images are obtained at the other two wavelengths. Images of O($^3P_1$) are

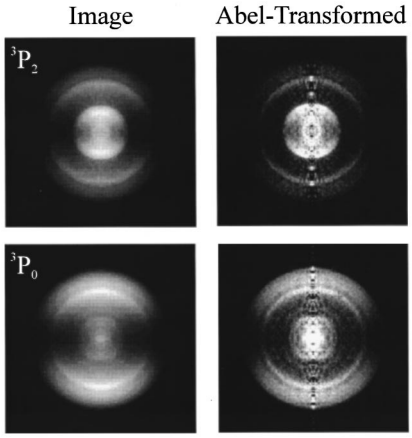

FIG. 3. Images of the $O(^3P_j)$ photofragments and their Abel transforms obtained from NO_2 photodissociation at 338.9 nm. $O(^3P_j)$, $j=0$ and 2 were detected by $(2+1)$ REMPI at 225.68 and 226.28 nm, respectively.

qualitatively similar to those of $O(^3P_{2,0})$ and therefore were not explored in detail. The fragment speed and angular distributions are derived from the Abel-transformed images. The speed distribution is obtained by integrating the signal at each distance (or velocity) over all angles. To obtain the angular distributions, the velocities within a prescribed small velocity range ΔV are summed.

For NO images, the angular distributions associated with $O(^3P_1)$ and $O(^3P_2)$ were determined by integrating over each ring's velocity width. Note that in these one-color experiments, probing each $NO(v,J)$ state is associated with a slightly different excess energy and this was taken into account in the analysis. The dependence of β on E_t in the range 0–400 cm^{-1} for $NO(J)$ correlated with $O(^3P_2)$ and $O(^3P_1)$ is summarized in Fig. 4 and Table I. Two trends are manifest: (i) the recoil anisotropy parameter β decreases with increasing rotational and decreasing translational energy; and (ii) at the same E_t, NO at higher J [correlated with $O(^3P_2)$] gives rise to lower β than NO at lower J [correlated with $O(^3P_1)$]. Thus, β depends both on rotational and translational energy of the fragments.

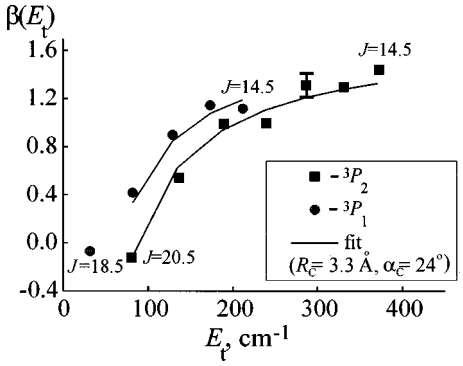

FIG. 4. Dependence of the anisotropy parameter β of $NO(^2\Pi_{1/2}, v=2, J)$ on the c.m. translational energy E_t for NO_2 dissociation around 338 nm. The squares and circles represent NO fragments correlated with $O(^3P_2)$ and $O(^3P_1)$, respectively. The solid line is the fit using the model described in the text; the highest NO J state associated with $O(^3P_1)$ is not included in the fit, because it can be generated only from NO_2, whose rotational state is greater than 0.5.

TABLE I. β values corresponding to $O(^3P_2)$ and $O(^3P_0)$ fragments obtained from the $NO(v=2, J)$ angular distributions. The uncertainty in β is ± 0.1

$Q_{21d}(J)$ J(NO)	Corresponding $O(^3P_j)$ state	E_{tr}, cm^{-1}	β(Imaging)	β(TOF)
$J=21.5$	$^3P_2$	21.27	···	−0.1
$J=20.5$	$^3P_2$	78.51	0.23	−0.2
$J=19.5$	$^3P_2$	134.42	0.68	0.2
$J=18.5$	$^3P_2$	187.47	0.96	1.1
	$^3P_1$	29.47	0.04	−0.1
$J=17.5$	$^3P_2$	237.5	1.05	1.0
	$^3P_1$	79.5	0.47	−0.2
$J=16.5$	$^3P_2$	284.94	1.47	1.2
	$^3P_1$	126.94	0.84	>0.3
$J=15.5$	$^3P_2$	329.35	1.34	1.3
	$^3P_1$	171.35	1.09	>0.3
$J=14.5$	$^3P_2$	370.84	1.48	1.3
	$^3P_1$	212.84	1.03	>0.4
$J=13.5$	$^3P_2$	411.22	···	1.3
	$^3P_1$	253.22	···	>0.4

Similar conclusions are drawn from analyses of the $O(^3P_j)$ images. The speed distribution of each $O(^3P_j)$, obtained by integration over all angles, has been converted to a translational energy distribution $P(E_t)$ which is related to the NO internal energy (vibrational, rotational, and spin-orbit) distribution $P(E_{int})$ by energy conservation. The $P(E_t)$ distributions of $O(^3P_2)$ and $O(^3P_0)$ obtained at 338.9-, 354.7-, and 371.7-nm are shown in Fig. 5.

The distinct peaks in the translational energy distributions are associated either with specific NO vibrational levels (whose thresholds are indicated by arrows), or with oscillatory structures in the rotational energy distribution of each $NO(v)$. The latter, which depend sensitively on excitation energy, are well documented and interpreted as signatures of bending vibrational structure of the transition state (TS).[14] The distributions obtained at 354.7 nm are in good agreement with previous results.[7,28,29] They reflect the structures of the $NO(v=0,1)$ rotational distributions, which have been measured directly by monitoring NO.[17,19,38] In particular, the bimodal energy distribution of $NO(v=1)$ at this wavelength, which has two distinct peaks at low and high J's, is well reproduced in the image. The differences between the $O(^3P_2)$ and $O(^3P_0)E_t$ distributions obtained at each photolysis wavelength are another manifestation of the fluctuations that are pervasive in NO_2 dissociation.[14]

In order to derive the dependence of β on E_t, the angular distributions of narrow rings of width ΔV are fit to Eq. (1). The results are shown in Fig. 6. Note that each measured β is a weighted average of the β parameters associated with the $NO(\Omega,v,J)$ states whose E_{int} is complementary to E_t. Also, the measured data result from a convolution with the apparatus resolution function.

The most remarkable feature in Fig. 6 is the similarity of the functional dependence of β on E_t at the three photolysis wavelengths, despite the large differences in excess energy and the corresponding NO rovibrational distributions. Likewise, at each of the three photolysis energies, the curves for the two measured oxygen spin-orbit states, $O(^3P_2)$ and $O(^3P_0)$, are similar. This is significant, since while $O(^3P_2)$

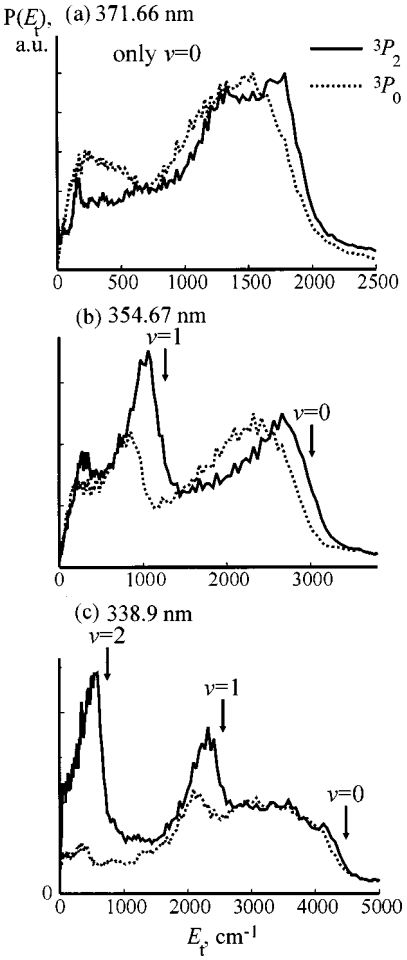

FIG. 5. Photofragment c.m. translational energy distributions obtained from $O(^3P_2)$ and $O(^3P_0)$ Abel-transformed images at the specified dissociation wavelengths. The arrows indicate the opening of each correlated NO vibrational level.

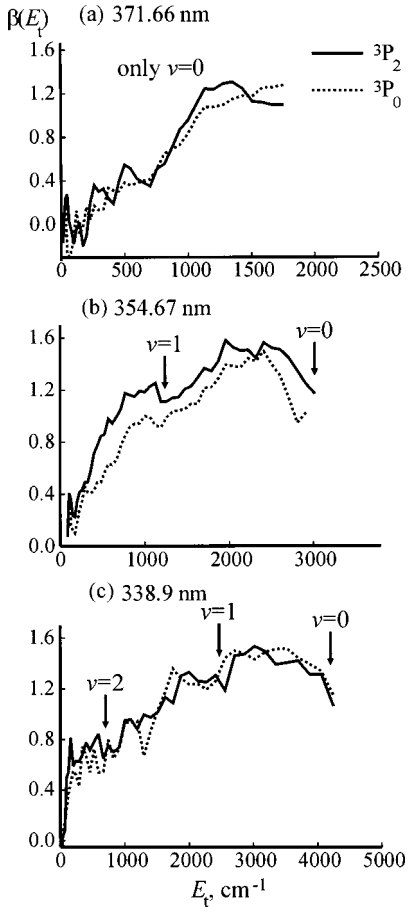

FIG. 6. The dependence of β obtained from the $O(^3P_2)$ and $O(^3P_0)$ Abel-transformed images on c.m. translational energy at the same dissociation wavelengths as in Fig. 5.

can be aligned, the projection of the $O(^3P_0)$ angular momentum on the quantization axis is zero and no alignment is possible. In a previous study at ~355 nm, $O(^3P_0)$ was found to exhibit less anisotropy than $O(^3P_2)$,[28] but this behavior is not reproduced in our study (see Fig. 6). Possibly, due to the very small population of $O(^3P_0)$,[14] some isotropic contamination contributed to the observed reduction in β in the previous study. The clear dependence of β on NO rotational level is evident in the 371.66-nm photolysis data where only $NO(v=0)$ is energetically allowed.

B. TOF spectra

The TOF data obtained at Georgia confirm the results obtained at USC. The one-color photolysis and detection requires focusing of the laser beam, which results in a small interaction volume. Therefore, a forward convolution procedure is applied to the analysis of the TOF spectra. Assuming an angular c.m. distribution described by even Legendre polynomials, the arrival time of the ions at the detector for all scattering angles Θ and ϕ is calculated. Because the ion optics does not preserve completely the cylindrical symmetry, it is necessary to include the ϕ dependence. The finite angular and velocity spreads of the molecular beam are simulated by Gaussian distributions of appropriate width. A strong correlation between the velocity direction of the parent molecule and the actual position of photolysis is assumed. The overall effect of these deviations from an ideal experiment can be well described by a convolution of the original TOF distribution with a Gaussian of full width at half-maximum (FWHM) 8%. In order to completely determine the kinematics of the fragmentation, we calculate the translational energy from energy conservation neglecting the (small) internal energy of the parent. With the current resolution, it is not possible to detect any indication of the modulation due to Legendre polynomials of degree larger than 2. A series of TOF profiles and their simulations are shown in Fig. 7.

The β parameter is determined by a least-squares fit to the data. Near the energetic threshold, the TOF spectra are sensitive to the different fine-structure states of the O atom. In these cases, we simulate the spectra as a superposition of two corresponding c.m. distributions with independent β values and amplitudes. With increasing E_t, the different spin-orbit states are less well resolved, resulting in strong correlation between the parameters. It is for this reason that we can only determine a lower limit for the anisotropy parameters for NO $v=2$, $J<17.5$. Furthermore, the resolution of the TOF experiment was not sufficient to resolve structures

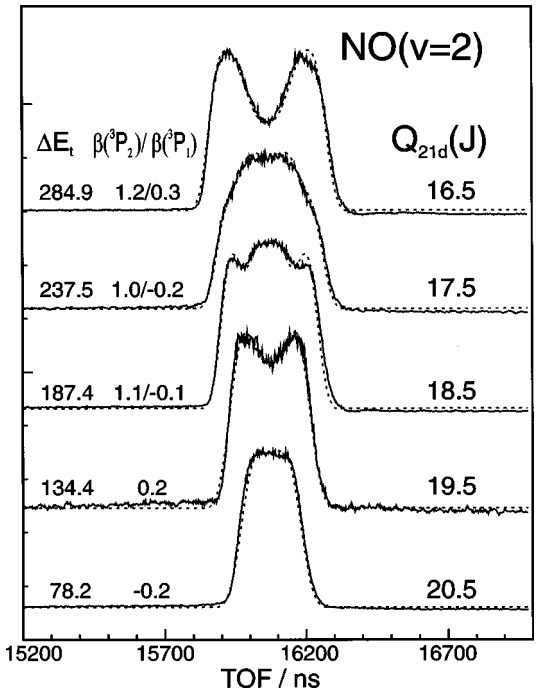

FIG. 7. TOF spectra of NO($X\,^2\Pi_{1/2}, v''=2, J$) resulting from the photodissociation of NO_2. The dashed curves represent fits to the experimental spectra assuming the indicated anisotropy parameters $\beta(^3P_2)$ and $\beta(^3P_1)$ associated with the two fine-structure components of the O(^3P) fragment. The spectra are taken with an acceleration voltage of 10 V/cm, laser energy 0.6 mJ, and 500-mm focal length lens. The available translational energy E_t (in cm^{-1}) for the NO+O($^3P_2$) channel is indicated for each spectrum.

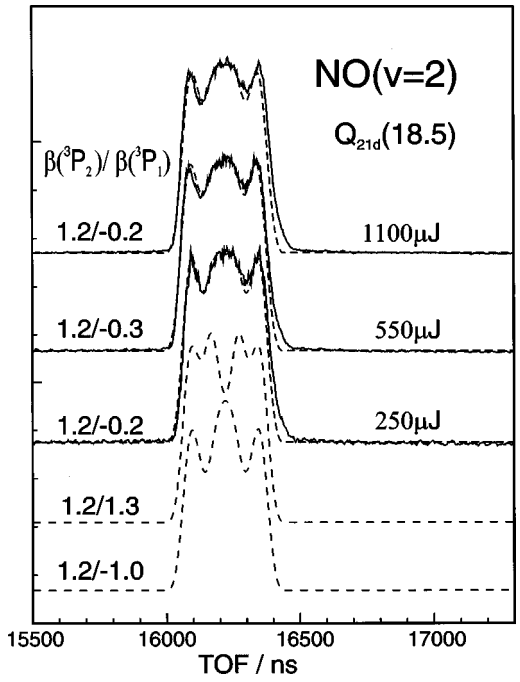

FIG. 8. TOF spectra of NO($X\,^2\Pi_{1/2}, v''=2, J=18.5$) recorded at the indicated laser pulse energies. The dashed lines represent simulations of the TOF spectra as described in the text. For the simulated spectra in the bottom part, we assumed the limiting anisotropy parameters $\beta=-1.0$ and $\beta=1.3$, respectively. All spectra are calculated using the amplitude ratio $\sigma(^3P_1)/\sigma(^3P_2)=0.4$.

due to the opening of the exit channel associated with the production of O($^3P_0$) fragments. Therefore this channel, which is open for NO($v=2$, $J<16.5$), is not included in the data analysis. The uncertainty in the β parameters is determined by the range of values that fit the experimental spectra, and is estimated at ± 0.1.

A summary of the β parameters is given in Table I. As in the imaging data, with increasing NO(J), a substantial reduction in the anisotropy parameter is evident. The deviations from the low-J limit can be detected only at $E_t < 300\,cm^{-1}$. very close to the thresholds for each O(^3P_j), we find very small and even negative β values, indicating substantial deviations from axial recoil.

C. Saturation behavior

In estimating the accuracy of the measured β parameters, especially in the one-color experiments that require high power densities, the effect of saturation has to be evaluated. Under the conditions of the present experiment, NO $(2+1)$ REMPI detection is characterized by quadratic power dependence indicating the two-photon absorption as the rate limiting step. On the other hand, a power dependence of less than 2.5 is found for the production of NO fragments in the one-color photodissociation of NO_2. The deviation from the ideal cubic power dependence could be attributed to saturation of the one-photon step in NO_2 photolysis. Depending on the competition between the optical pumping and dissociation rates, we expect a loss of anisotropy for the state resolved fragment velocity distributions. To check these effects, we measured product TOF spectra for different laser pulse energies. Typical results for $J=18.5$ are shown in Fig. 8. The derived anisotropy parameters changed by less than 0.1 when the laser pulse energy was increased by a factor of 4. Furthermore, a substantial part of the reduction was due to space-charge effects. This somewhat puzzling result can be readily understood when the classical optical pump rate is compared with the dissociation rate. The radiative lifetime for the parallel electronic transition is $<1\ \mu s$,[40] and we estimate for our experiment an optical pump rate corresponding to a pump cycle of at least 15 ps. This value must be compared with the subpicosecond lifetime of NO_2 with excess energies $>1500\ cm^{-1}$.[21] At the higher excess energies investigated here, the lifetime is even shorter. Thus, dissociation is clearly the fastest process, and the deviations from the cubic power dependence must therefore be attributed to a depletion of the NO_2 density in the laser photolysis/probe volume, which should not affect the value of β.

IV. CLASSICAL MODEL FOR NONAXIAL FRAGMENT RECOIL

A. Transverse recoil derived from angular momentum conservation

The classical model presented below for NO_2 dissociation is based on energy and angular momentum conservation,

$$h\nu - D_0 = E_{\rm int}^{\rm NO} + E_t^{\rm NO} + E_t^{\rm O} + E_{\rm el}^{\rm O}, \tag{4}$$

$$\mathbf{J}_{\rm NO_2} = \mathbf{J}_{\rm NO} + \mathbf{J}_{\rm O} + \mathbf{L}, \tag{5}$$

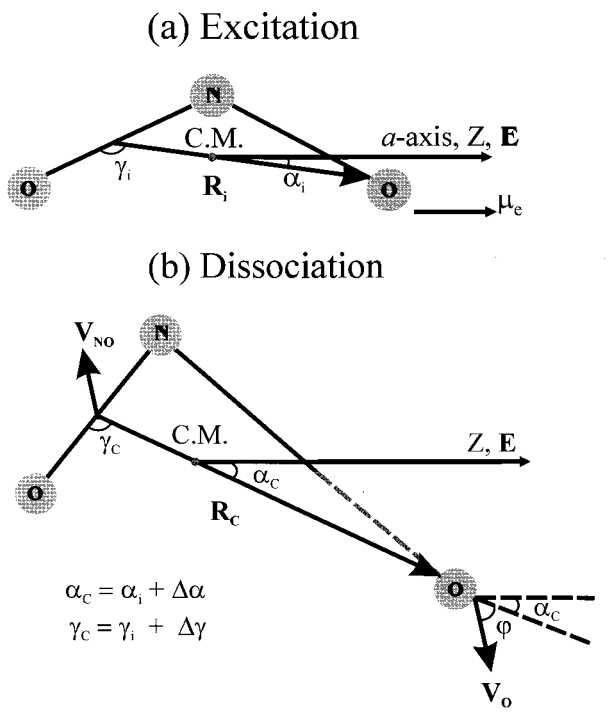

FIG. 9. (a) Geometry of the NO_2 molecule prior to photoexcitation indicating the orientation of the transition dipole moment vector $\boldsymbol{\mu}_\varepsilon$, the laser polarization vector **E**, and the initial angle α_i between **R** and **E**. (b) Geometry and orientation of NO_2 after evolving from the initial to the critical configuration. The angle φ dictated by angular momentum conservation determines the deviation from axial recoil. Notice that the change in γ determines the change in the angle α.

where D_0 is the dissociation threshold of NO_2, E_t^{NO} and E_t^O are the c.m. recoil energies of the fragments; E_{el}^O is the electronic energy of the spin-orbit state of the O atom; E_{int}^{NO} includes the vibrational, rotational, and spin-orbit energies of the NO fragment; $\mathbf{J}_{NO_2}$, $\mathbf{J}_{NO}$ and $\mathbf{J}_O$ are the angular momenta of the parent NO_2 molecule, and NO and O fragments, respectively; and **L** is the orbital angular momentum. The model applies to triatomic dissociation induced by optical transitions that lie in the molecular plane. In common with all classical models, it is valid when the product angular momentum is high. In our case, $J_{NO_2}=1/2$ and 3/2 and thus J_{NO_2} and J_O can be neglected, and J_{NO} is balanced mainly by L. Note that for a fixed photolysis energy, high J_{NO} states correlate with low recoil energy ($E_t=E_t^{NO}+E_t^O$) and high L.

Jacobi coordinates are chosen to describe the dissociation in the molecule fixed frame (MFF); i.e., R is the distance from the departing O atom to the c.m. of NO, r is the internuclear distance in NO, and γ is the angle between **R** and **r** (Fig. 9). During dissociation, NO rotation, which is in the parent plane, is accompanied by a counter-rotation of **R** around the c.m. of NO_2, in order to conserve angular momentum.

Notice that in contrast to direct triatomic dissociation, where the anisotropy in the angular potential is the main source of torque, in vibrational predissociation from a barrierless PES, the main source of diatom angular momentum is bending vibrations in the TS.[14,41] Irrespective of the source of angular momentum, however, the fundamental conservation laws must be obeyed, and they impose restrictions on product trajectories. In the c.m. coordinate system, the classical orbital angular momentum is given by [Fig. 9(b)],

$$\mathbf{L}=m_{NO}\mathbf{r}_{NO}\times\mathbf{V}_{NO}+m_O\mathbf{r}_O\times\mathbf{V}_O, \tag{6}$$

where $\mathbf{r}_{NO}$ is the vector directed from the c.m. of NO_2 to the c.m. of the NO fragment, $\mathbf{V}_{NO}$ is the c.m. velocity of NO, and $\mathbf{r}_O$ and $\mathbf{V}_O$ are the corresponding quantities for the O atom. Momentum conservation dictates that

$$\mathbf{L}=m_O\mathbf{R}\times\mathbf{V}_O, \tag{7}$$

which is equivalent to the classical expression for the orbital angular momentum in terms of the long-range impact parameter b, $L=\mu Vb$, where $\mu=m_{NO}m_O/(m_{NO}+m_O)$ is the reduced mass and V is the relative velocity of the recoiling fragments. If we define axial recoil as the recoil of a diatomic fragment in a direction that correlates with no angular momentum in the fragment, then the direction of the recoil must coincide with **R**. Consequently, we relate axial and transverse recoil to the direction of **R**.

Using $|\mathbf{J}|=\hbar\sqrt{J(J+1)}$ and $|\mathbf{L}|=m_OR_CV_O\sin\varphi=\mu VR_C\sin\varphi$, where φ is the angle between **R** and $\mathbf{V}_O$, and R_C is a critical distance where the angular momenta become established, we obtain

$$m_OR_CV_O\sin\varphi=\hbar\sqrt{J(J+1)}. \tag{8}$$

Defining $E_{avl}=h\nu-D_0-E_{el}^O-E_{vib}^{NO}=E_t+E_{rot}$ as the total fragment rotational and translational energy associated with each NO(v) product, this expression can be written as

$$\sin^2\varphi=\frac{\mu_{NO}\cdot r^2}{\mu\cdot R_C^2\cdot\left(\dfrac{E_{avl}}{E_{rot}}-1\right)}. \tag{9}$$

Equation (9) highlights the conditions necessary for large deviations from axial recoil (large φ): (i) E_{avl}/E_{rot} cannot be too large compared to 1. In other words, E_{rot} must constitute a large fraction of E_{avl}; and (ii) $I_{NO}=\mu_{NO}r^2$ must be comparable to $I_{NO_2}=\mu R_C^2$ at the critical distance R_C where the angular momenta have reached their final values.

In applying the model to NO_2 dissociation, we adopt the following geometrical configuration of the ground state. The equilibrium ONO bond angle is 134°, and the NO bond lengths are both equal to $r=1.189$ Å[42]; this corresponds to $R=1.692$ Å and $\gamma=152°$. The choice of the critical distance R_C is less certain. We define it as the distance at which the NO product has developed its final free rotational state, and consequently the orbital angular momentum must be established as well. This value can be loosely related to the value of R at the TS; i.e., $R_C\geqslant R_{TS}$. Relying on recent calculations of the NO_2 PES and statistical [variational Rice–Ramsperger–Kassel–Marcus (RRKM)] calculations that have determined the location of the TS and its geometry as a function of excess energy,[23,43,44] we use $R_C\geqslant 2.7$ Å, $r=1.189$ Å, and $\gamma\sim 120°$ (corresponding to ONO TS angle of $\sim 109°$).[43]

From Eqs. (8) and (9) it is evident that at each E_{avl}, a specific fragment quantum state will be associated with a distinct transverse recoil angle φ, and the deviations from axial recoil will increase with increasing E_{rot} (and concomitantly decreasing E_t). Also, in accordance with angular mo-

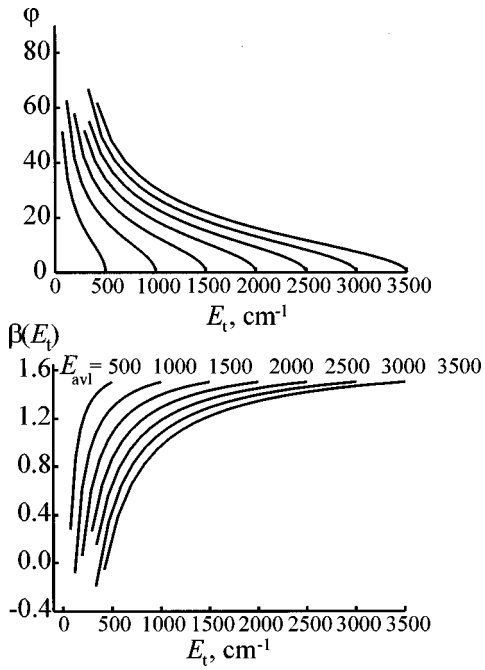

FIG. 10. Final fragment recoil angle φ (top) and anisotropy parameter β (bottom) plotted as a function of the c.m. translational energy E_t, calculated for different values of the available energy E_{avl} (defined as the total available translational and rotational energy of the fragments). $R_C=3.3$ Å and $\alpha_C=27°$ were used in these simulations (see the text).

mentum conservation, at a given E_{avl} and R_C, there is a maximum value of product J that is allowed.

The dependence of φ on E_t is illustrated in Fig. 10 for a series of E_{avl}, using the NO_2 parameters given above. Clearly, this dependence becomes much steeper at low E_t. At the bottom, we illustrate the corresponding changes in β, assuming $\beta=1.6$ for pure axial recoil (see below). As expected, β decreases strongly at small E_t, and may even assume negative values.

The limiting value of β associated with axial recoil needs comment. In an electronic transition with B_2 symmetry, the transition dipole moment $\boldsymbol{\mu}_{\boldsymbol{\varepsilon}}$ lies parallel to the figure axis, or the a axis of a prolate top. When R is parallel to the a axis, $\beta=2.0$, but when R deviates from the a axis, $\beta<2.0$ will be obtained even for fast dissociation, generating a diatom with no angular momentum. Defining α as the angle between R and the a axis, we obtain the usual expression,[1,18]

$$\beta=2P_2[\cos(\alpha+\varphi)]. \tag{10}$$

Thus, in a parallel transition with $\alpha\neq 0$, $\beta<2.0$ is observed even for pure axial recoil ($\varphi=0$). The results obtained by using Eq. (10) with $\alpha=24°$ and positive φ (corresponding to clockwise rotation) are shown in Fig. 10(b).

B. Applications of the model

Although the model described above is general, its implementation for predissociating systems is not always straightforward. On the one hand, the large degree of rotational excitation justifies the classical treatment. On the other hand, the geometrical configurations at which the model is applied are often ill defined. In particular, R_C and α_C are unknown, and must be either inferred from fits to the data, or obtained from calculations. Below, we discuss two cases, one in which we compare our model to results of quantum calculations for Ne–ICl predissociation, and the other—an application to the NO_2 decomposition results reported here.

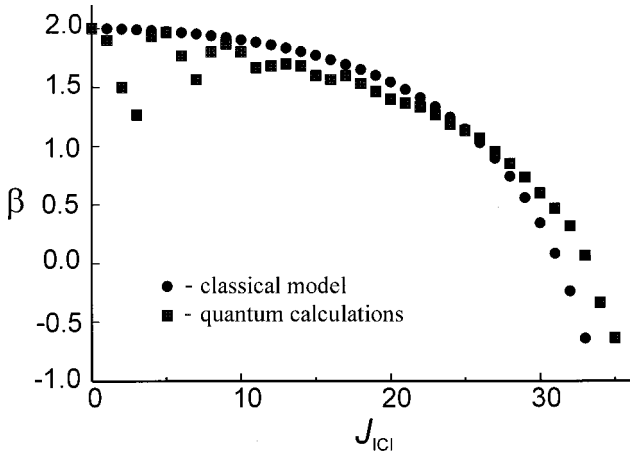

FIG. 11. Dependence of β in the vibrational predissociation of Ne–ICl on the rotational state of the ICl fragment, obtained from the quantum calculations of Ref. 4 (squares), and calculated from the classical model (circles). See the text for details.

1. Ne–ICl vibrational predissociation

As a first application, we calculate the expected deviations from axial recoil in the predissociation of the Ne–ICl complex following photoexcitation to its B electronic state that correlates with the $B\,^3\Pi_{0+}$ state of the ICl product,[4]

$$\mathrm{Ne{-}ICl}(X,v=0,\ J_{\mathrm{Ne{-}ICl}}=0)\rightarrow \mathrm{Ne{-}ICl}(B,v=2,\ J_{\mathrm{Ne{-}ICl}}=1)\rightarrow \mathrm{Ne}+\mathrm{ICl}(B,v=1,\ J_{\mathrm{ICl}}). \tag{11}$$

For this complex, the ICl rotational distributions were determined experimentally.[45] Quantum calculations of the ICl rotational distribution, as well as the dependence of the β parameter on the ICl final rotational state, J_{ICl}, were carried out using an empirical PES.[4]

Optical excitation prepares an isolated resonance centered at 42.31 cm^{-1} above the ICl($B,v=2,\ J_{\mathrm{ICl}}=0$) asymptote via a transition whose dipole moment is nearly parallel to **R** of the bent Ne–ICl complex. The resonance in the excited state is coupled to the continuum via vibrational predissociation, and projects onto J_{ICl} of the ICl(B) state. The calculated ICl($v=1$) rotational distribution ($E_{\mathrm{avl}}=140.4\,\mathrm{cm}^{-1}$) is similar to the one obtained experimentally and spans $J=0-35$.[4,45] The β parameter calculated quantum mechanically is nearly 2.0 for low J's, but decreases substantially for higher J's (see Fig. 11). Since Ne–ICl predissociation falls nicely within the criteria identified for nonaxial recoil [Eq. (9)], the classical model should show how much of the β variation with J obtained in the quantum calculations is due to transverse recoil.

In our calculations we used $R_C=4.95$ Å, which is the location of the top of the calculated potential barrier.[4] We assume $\alpha=0$ throughout the dissociation process, since $\beta=2$ is found for low J_{ICl}. The comparison with the results of

the quantum calculations is shown in Fig. 11. The good agreement between the quantum calculations at $J_{\mathrm{ICl}}>10$ indicates that the predominant reason for the strong decrease in β as a function J_{ICl} is the transverse recoil that must accompany the dissociation into high fragment J (and low E_t) states. Angular momentum conservation is included explicitly in the quantum calculations.[4]

2. Implementation of the model to NO_2 unimolecular reaction

The main differences between the Ne–ICl example and the NO_2 case are that for NO_2, α and R_C are treated as fitting parameters, and the transverse recoil angle φ can be either added to or subtracted from α. In the former case, a decrease in β for all values of φ should be observed. In the latter case, β will increase until α-φ reaches zero (or $\mathbf{V}_0$ coincides with $\mathbf{R}$), and then decrease as $\mathbf{V_0}$ and $\mathbf{R}$ diverge. In the absence of dynamical information, we chose to use an equal weighting of both, namely,

$$\beta_{\mathrm{av}}=[P_2(\cos(\alpha+\varphi))+P_2(\cos(\alpha-\varphi))]. \tag{12}$$

This choice is sensible, since the main source of fragment rotational angular momentum in NO_2 dissociation at energies not too close to D_0 is bending vibrations in the TS.[14] Invoking a separation of the motions perpendicular to the reaction coordinate and the harmonic approximation, we give equal weighting to inward and outward bending motions (corresponding to positive and negative φ), which evolve into clockwise and counterclockwise rotation of $\mathbf{R}$, respectively. We note that the use of Eq. (12) yields better fits to the data than using solely $+\varphi$ or $-\varphi$, although the fits are not sensitive to the exact weighting factors in Eq. (12). The data shown in Fig. 4 are best fit (using $J_{\mathrm{NO_2}}=1/2$) with $\alpha_C=24°$, and $R_C=3.3$ Å.

The model simulations of the β variation in the $O(^3P_j)$ images were performed as follows. The corresponding NO internal energy distributions were taken either from phase space theory (PST) calculations using the separate statistical ensembles method (SSE),[46,47] or from experiments in which the NO rovibrational distributions were measured directly.[14,17,19,38] The NO internal energy distributions were convoluted with the instrument resolution function, and the final β values were calculated as the weighted averages of the individual β values for the NO v,J states, whose energies correspond to E_t values that fall within a small range ΔE_t.[48]

The simulations of the $O(^3P_2)$ results are shown in Fig. 12. $R_C=3.3\pm0.3$ Å gives the best fit for all the data sets. At 371.7 nm we obtain $\alpha_C=30°$, and since only NO($v=0$, J) can be produced, the NO rotational distributions in the simulations are generated by PST. At 354.7 nm, experimental data for the NO rovibrational distributions are available, and the distributions measured by Reisler and co-workers are used as input in the simulation.[14,19] However, using PST/SSE to calculate the NO distributions yields an equally good fit, both with $\alpha_C=24°$. The small increase in β near the threshold for the opening of $v=1$, which is apparent both in the experimental data and the simulations, and has been observed before,[28] illustrates that at the same E_{avl}, $v=1$ (which has much less rotational excitation than $v=0$) gives rise to a slightly higher value of β. The 338.9-nm data are best fit with $\alpha_C=27°$. Here, $v=2,1$, and 0 are generated, and the distributions are calculated by PST/SSE, since no experimental data are available.[49] In summary, the simulations fit the data with rather similar choices of R_C and α_C, and exhibit large contributions of transverse recoil for high J states.

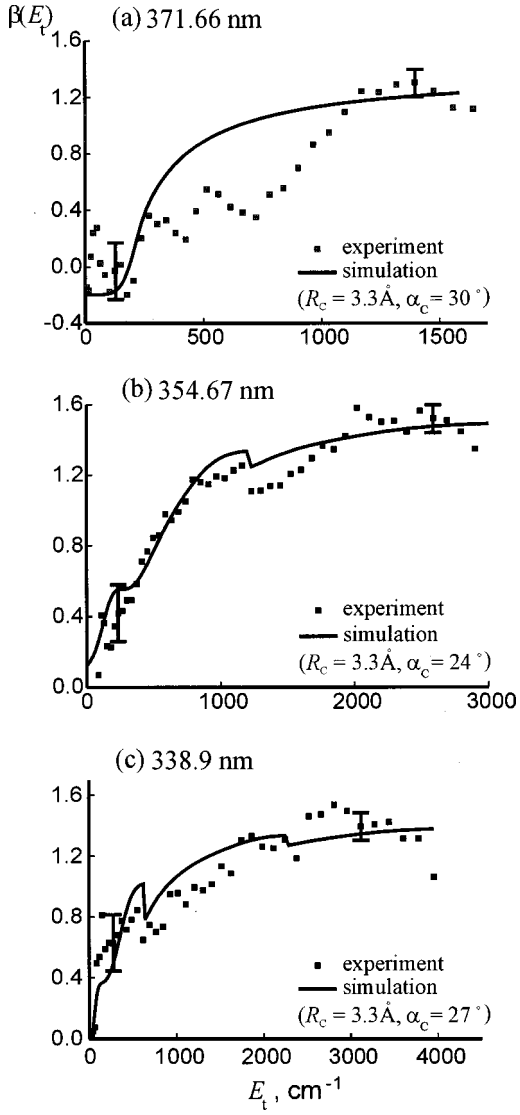

FIG. 12. Simulations of the dependencies of β obtained from $O(^3P_2)$ images on c.m. translational energy for the three experimental dissociation wavelengths as in Figs. 5 and 6. The values of R_C and α_C that best fit the data for each wavelength are indicated. See the text for details. The error bars represent uncertainties in β in the region of high and low E_t.

V. DISCUSSION

A. Implications to NO_2 photodissociation dynamics

The two parameters of the model, R_C and α_C, are relevant to the mechanism of NO_2 dissociation. Recall that in order to calculate β, α and R must be related to the space fixed frame (SFF), which is determined by the laser polarization vector $\mathbf{E}$.[1,2] Our model is based only on conservation laws and does not take into account (at least explicitly) any particular nuclear motions during dissociation.

In barrierless dissociation, the location of the TS is not sharply defined and is known (e.g., by variational RRKM calculations) to move inward with increasing excess energy.[23,24] For NO_2 at high excess energies it is located around 2.7 Å,[24,43] and thus the value of R_C that best fits the data, $R_C = 3.3$ Å, is reasonable. It is located between the calculated value of the TS (2.7 Å) and the location of the centrifugal barriers (4–5 Å), beyond which no further energy exchange among fragment states is expected. This R_C value also allows the population of the highest observed NO rotational levels. Note that at high E_t, β values close to the limiting axial-recoil value are obtained, and these are not very sensitive to the choice of R_C.

The angle α_C between the recoil velocity vector and **E** obtained from the fits is $\alpha_C = 27 \pm 3°$. In order to understand its origin, it is useful to distinguish between the excitation and dissociation steps. The ground-state equilibrium geometry of NO_2 determines the initial angle α_i between **R** and the *a* axis at the moment of excitation [Fig. 9(a)]. The initial bending angle $\gamma_i = 152°$ (see above) corresponds to $\alpha_i = 7.4°$, and therefore **R** must rotate during the dissociation with respect to the SFF to achieve the value of α_C that best fits the data. This added rotation should correlate to nuclear motions during the dissociation, which, in turn, must conserve angular momentum.

The most likely source of the change in α is a change in γ during dissociation. Since the parent angular momentum is nearly zero, the relative rotations of **r** and **R** in the molecular plane that determine γ must be correlated. In other words, in order to conserve angular momentum, any rotation of **R** (with angular velocity $\omega_R = d\varphi_R/dt$) must be compensated by a counter-rotation of **r** (with angular velocity $\omega_r = d\varphi_r/dt$). For a nonrotating parent molecule we obtain

$$\frac{d\varphi_r}{dt} = -\frac{d\varphi_R}{dt} \cdot \frac{\mu R^2}{\mu_{NO} r^2} = -\frac{I_{NO-O}}{I_{NO}} \cdot \frac{d\varphi_R}{dt}, \tag{13}$$

where I_{NO-O} and I_{NO} are the relevant moments of inertia. The time rate of change of γ is the combined rate of change of **R** and **r**, or,

$$\frac{d\gamma}{dt} = \frac{d\varphi_R}{dt} - \frac{d\varphi_r}{dt} = \left(1 + \frac{\mu R^2}{\mu_{NO} r^2}\right) \cdot \frac{d\varphi_R}{dt}. \tag{14}$$

Since rotation of **R** gives rise to a change in α [Fig. 9(b)], Eq. (14) yields

$$d\alpha = d\varphi_R = \frac{\mu_{NO} r^2}{\mu_{NO} r^2 + \mu R^2} d\gamma. \tag{15}$$

If the minimum energy path (MEP) in the (R, γ) plane is known [i.e., $R = R(\gamma)$ and $r = r(\gamma)$ are known], it is then possible to integrate Eq. (15), provided $\gamma(t)$ is known, and obtain the cumulative change in α,

$$\Delta\alpha = \int_{\gamma_i}^{\gamma_C} \frac{\mu_{NO} r^2}{\mu_{NO} r^2 + \mu R^2} d\gamma, \tag{16}$$

where γ_C is the angle γ at the moment of bond cleavage.

Equation (16) relates the deformation of the molecule in the MFF to the rotation of **R** in the SFF. The final value of $\alpha_C = \alpha_i + \Delta\alpha$ depends on the change in the nuclear configuration along the MEP expressed relative to the SFF. For a given change in γ, the corresponding change in α depends on the ratio between I_{NO-O} and I_{NO}. In other words, substantial rotation of **R** can be achieved only when I_{NO-O} is comparable to I_{NO}. Thus, we must assume that the change in γ from its equilibrium value (152°) to its final value (~125°) occurs at a relatively small *R*, and is then followed by additional stretching of *R* (or the dissociating NO bond) until the critical distance R_C is reached.

We can now compare the motions suggested by our model to those predicted or calculated for NO_2. The changes in nuclear configuration during dissociation can be related to the geometry of the conical intersection that couples the $^2A_1$ and $^2B_2$ states, and/or to the curvature of the ground-state MEP in the (R, γ) plane. Calculations show that the conical intersection occurs at an angle $\gamma \cong 120°$,[15,16] while recent ab initio calculations of the ground-state PES find that in the TS region $\gamma = 123°$,[43] a value close to that required for the conical intersection. Moreover, in the most recent ab initio calculations, it is shown that the MEP in the (R, γ) plane is significantly curved only for $R < 2.1$ Å reaching angles of 120–130°, while at larger *R*, the MEP can be described by pure stretching motion up to the TS.[44] Thus, most of the change in γ occurs at small *R*, and the bending angle for the conical intersection happens to be similar to that in the TS region. Trajectory calculations using the method described by Loock *et al.*,[9] and carried out on an analytical PES whose shape has similar characteristics to the NO_2 PES calculated ab initio, also confirm that the expected changes in β on such a PES are similar to those observed experimentally.

Does the closing of γ reflect dynamics on the ground $^2A_1$ state, excited $^2B_2$ state, or both? Near threshold, it is established that dissociation evolves mostly on the ground electronic state, and the dissociation time is longer than a picosecond. Thus, at the near threshold energies (0–128 cm^{-1}) explored by Butenhoff and Rohlfing,[27] changes in geometry during dissociation must relate to the dynamics on $^2A_1$. The situation is more complicated at the high excess energies (2000–4000 cm^{-1}) employed here. Since the dissociation lifetime is much shorter than a picosecond, many overlapping resonances are excited coherently, even with a nanosecond laser. Therefore, the excited dissociation wave function may initially contain a significant $^2B_2$ character, which will dephase into the ground state. Recent time-dependent calculations estimate the dephasing time at 50–90 fs (the duration of few bending periods),[50] which is probably not much shorter than the dissociation time. Consequently, it is not guaranteed that the initial coherent superposition of resonances launched at the crossing seam will behave in an ergodic fashion en route to dissociation. In other words, the dissociative trajectories may be influenced by the PES at the crossing seam. Our experiments cannot distinguish between these different scenarios; they do suggest, however, that the reduction in the bending angle γ must occur near the Franck–Condon region.

B. Deviations from axial recoil in unimolecular decomposition

In this section we discuss the requirements for observing changes in β in photodissociation dynamics due to transverse recoil. Clearly, an in-plane optical transition (parallel or perpendicular) is required. Several conditions are apparent by inspection of Eq. (9). First, large deviations from axial recoil should be observed when the c.m. axial-recoil velocity component is small compared to the tangential velocity component induced by the rotation of the diatomic fragment. This means that in fast barrierless unimolecular dissociation, where typically the kinetic energy release is small and fragment rotational excitation often extends to E_{avl}, such deviations should be routinely observed. Second, the nonaxial recoil, which has a $\sin\varphi$ dependence, increases sharply as E_{rot} approaches E_{avl}; in other words, the highest J states will exhibit particularly large deviations. Third, the moment of inertia of the diatom should be comparable to the moment of inertia associated with the orbital motion; i.e., R_C cannot be too large when the reduced masses related to r and R are similar. This condition is also necessary for the generation of a significant change in the angle α during dissociation.

Pursuant to the above, it is straightforward to predict systems for which a correlation of β with diatomic rotation will be observed. The change of β is expected to be large for vibrational predissociation, and for direct dissociation accompanied by substantial fragment rotational excitations. Some examples are Ne–ICl, NO_2, O_3, N_2O, SO_2, and Cl_2O. The 193-nm photolysis of NH_3 via a conical intersection also falls nicely into this category, and the model suggested by Mordaunt *et al.* demonstrates how β can change from a limiting value of -1 to positive values.[10] Their model is also based on angular momentum conservation, and has common features with the model presented here. In certain cases, the ratio of the moments of inertia given in Eq. (9) is not favorable; for example, in ICN, BrCN, CINO, and BrNO. Indeed, in the 266-nm photodissociation of ICN and the 355-nm photolysis of CINO, no dependence of β on fragment rotation has been observed.[51,52]

We emphasize that the effect described here is by no means the only one to cause deviations from the limiting value of β. It has already been demonstrated that specific exit-channel dynamics either involving surface crossings or in- and out-of-plane nuclear motions during the dissociation, as well as alignment effects and polarization of the m_J distributions, can cause large deviations from the limiting values. For example, in a recent work on the photodissociation of NO_2 at 212.8 nm, orbital alignment in the oxygen atom has been observed.[53] However, even when other effects are important, the deviations from axial recoil resulting from conservation of angular momentum must be subtracted from the data before the importance of other parameters can be assessed.

Finally, a comparison of the classical treatment of β with the quantum mechanical formulation is enlightening. G. G. Balint-Kurti and M. Shapiro provided one of the first quantum mechanical expressions of β for a triatomic dissociation initiated with linearly polarized light.[3] Beswick and coworkers later gave a more general formula including cases involving excitation by circularly polarized light.[4] They also provided a simplified formula of β corresponding to the initial parent molecular state with a zero angular momentum $J_i=0$. In this case, β can be expressed as

$$\beta(J)=\frac{(2\mu_0^2-\mu_+^2-\mu_-^2)}{(\mu_0^2+\mu_+^2+\mu_-^2)}, \tag{17}$$

where $\mu_0^2=|\langle 0\|\boldsymbol{\mu}_{\boldsymbol{\epsilon}}\|1,J,0\rangle|^2$, and $\mu_\pm^2=|\langle 0\|\boldsymbol{\mu}_{\boldsymbol{\epsilon}}\|1,J,\pm 1\rangle|^2$ are the reduced matrix elements of the transition dipole moment as defined in Ref. 4, $\langle 0|$ is the initial parent wave function, and $|J_f,J,\Omega\rangle$ is the dissociation wave function with final state total angular momentum $J_f=1$, angular momentum of the diatomic fragment J, and a projection $\Omega=0$ or ± 1 of $J_f=1$ on the z axis (along **R** of the dissociation fragments).

Based on this expression, it can be concluded that when $\mu_0^2=0$, $\beta=-1$ is obtained (a perpendicular transition), while $\mu_\pm^2=0$ but $\mu_0^2\neq 0$ corresponds to $\beta=2$ (a parallel transition). These two limiting cases correspond to transition dipole moments that are perpendicular and parallel to **R**, respectively. It is important to point out that Eq. (17) has no explicit dependence on product J state. A J-dependent β therefore implies that the reduced transition dipole matrix elements are functions of J.

In quantum mechanical treatments, observables are usually related to the quantization axis rather than to the parent molecular plane. Therefore, the physical interpretation of the reduced transition dipole matrix elements obtained in the close coupling calculations is not readily apparent, and it is difficult to glean the origin of the dependence of β on J. The classical treatment presented here, although valid only in the high J limit, nevertheless gives a simple and clear physical picture of the β changes. Assuming no rotation of **R** during dissociation, the quantum mechanical treatment for $J_f=1$ implies that when the transition dipole moment lies along **R** (the z axis), $\mu_0^2\neq 0$ and $\mu_\pm^2=0$. The dissociation process may lead to a decrease in μ_0^2 and an increase in the $\mu_\pm^2$ component with increasing fragment rotational quantum number. This mixing of the $\Omega=0$ and ± 1 components has been called Coriolis coupling in the quantum treatment,[4] whereas in the classical picture we show that it is a result of conservation of angular momentum in the molecular frame. When the initial transition dipole moment lies in the molecular plane, but is perpendicular to the direction of final recoil, $\mu_\pm^2\neq 0$ and $\mu_0^2=0$ are expected in the absence of ransverse recoil. Likewise, if dissociation proceeds with extensive transverse recoil, it is expected that there will be an increase in μ_0^2 and a decrease in $\mu_\pm^2$ as the fragment rotational quantum number is increased. This corresponds to a change of β from -1 toward 2, as J increases. Both cases were demonstrated in the quantum mechanical calculations of Beswick and co-workers (as displayed in Fig. 3 of Ref. 4). As shown above for the Ne–ICl dissociation, the dependence of β on ICl rotation obtained with the quantum mechanical calculation agrees well with the results of our classical model (Fig. 11). It is important to point out that each fragment J state is associated with a different recoil direction. A detailed quantum mechanical treatment is beyond the scope of this paper, but new calculations that treat this effect explicitly would

provide additional insights into the quantum origin of the effect.

VI. SUMMARY

A classical model is presented that describes nonaxial fragment recoil in unimolecular decomposition of triatomic molecules. The model is based on conservation of angular momentum, and predicts large deviations from axial recoil when (i) the c.m. translational energy of the recoiling products is small compared with the rotational energy of the diatomic fragment (i.e., $E_t \ll E_{\rm rot}$); and (ii) the moment of intertia of the diatomic fragment is comparable to that associated with the orbital motion. The two parameters needed to determine the nonaxial recoil are the interfragment separation R_C at the moment when the angular momenta are established, and the corresponding average angle α_C between $\mathbf{R}$ and $\mathbf{E}$ (or $\boldsymbol{\mu}_\varepsilon$ at the moment of excitation). Deviations from the limiting β values should be prominent in fast unimolecular decomposition, and in direct dissociation when a large fraction of $E_{\rm avl}$ is deposited in $E_{\rm rot}$. In these cases the contribution of axial recoil should be evaluated before other vector correlations are examined.

The application of the model to the unimolecular decomposition of NO_2 describes well the dependence of β on NO(J) and O(E_t), as observed in our work as well as by other investigators. The best fit is obtained with $R_C = 3.3 \pm 0.3$ Å and $\alpha_C = 27 \pm 3°$, implying that the dynamics during dissociation involve a reduction of the ONO bending angle in the Franck–Condon region followed by bond stretching. Such reduction is compatible with the geometry of the conical intersection between the $^2B_2$ and $^2A_1$ states, and with the calculated anisotropy of the ground-state PES.

(3) Comparison of the classical model with quantum mechanical calculations of the predissociation of the Ne–ICl complex indicates that the main source of the transverse recoil of the ICl fragment is the orbital angular momentum associated with high product J states. This case illustrates the correspondence between the classical and quantum treatments.

ACKNOWLEDGMENTS

The authors wish to thank A. Sanov, I. Bezel, W. Kim, and C. Wittig for helpful discussions. This work was supported by NSF Grant Nos. CHE-9632519 (H.R.) and CHE-9707670 (H.M.), and an NSERC grant (C.Q.). C.Q. also acknowledges a Visiting Fellowship from JILA, University of Colorado, Boulder.

APPENDIX: VECTOR CORRELATIONS AND THE TWO-PHOTON $H \leftarrow X$ TRANSITION IN NO

The two-photon transition, $H \leftarrow X$, is sensitive to a possible rotational angular momentum alignment due to the presence of a small second-rank tensor component. The angular dependence of the rotational quadrupole moment, $T_0^{(2)}(\Theta)$, is characterized by even Legendre polynomials of degree $\leqslant 4$, while the rotational hexadecapole moment, $T_0^{(4)} \times(\Theta)$, is modulated by polynomials of degree 2, 4, and 6. Each term in the expansion is weighted with a coefficient $C_\lambda^{(Q)}$ that depends on the angular momenta of the parent molecule, the fragments, as well as the different possible electric dipole transition moments.[35]

$$T_0^{(0)}(\Theta) = C_0^{(0)} + C_2^{(0)} P_2(\cos\Theta),$$

$$T_0^{(2)}(\Theta) = C_0^{(2)} + C_2^{(2)} P_2(\cos\Theta) + C_4^{(2)} P_4(\cos\Theta),$$

$$T_0^{(4)}(\Theta) = C_2^{(4)} P_2(\cos\Theta) + C_4^{(4)} P_4(\cos\Theta) + C_6^{(4)} P_6(\cos\Theta).$$

It is interesting to note that without resolving the angular distribution, the rotational alignment moment $T_0^{(2)}$ is determined by the coefficient $C_0^{(2)}$, whereas the angular anisotropy can only be influenced by a nonvanishing rotational alignment through the coefficients $C_2^{(2)}$ and $C_4^{(2)}$. Therefore, our findings are consistent with the possibility of detecting strong rotational alignment due to the coefficient $C_0^{(2)}$ while the corresponding state and angularly resolved product distributions do not show a significant contribution from a fourth Legendre polynomial $P_4(\cos\Theta)$. On the other hand, the effective anisotropy parameter will contain a contribution from the rotational quadrupole alignment moment due to the coefficient $C_2^{(2)}$.

[1] See, for example, R. J. Gordon and G. E. Hall, Adv. Chem. Phys. **XCVI**, 1 (1996).
[2] (a) R. N. Zare and D. R. Herschbach, Proc. IEEE **51**, 173 (1963); (b) R. N. Zare, Mol. Photochem. **4**, 1 (1972).
[3] G. G. Balint-Kurti and M. Shapiro, Chem. Phys. **61**, 137 (1981).
[4] O. Roncero, P. Villarreal, G. Delgado-Barrio, N. Halberstadt, and J. A. Beswick, J. Phys. Chem. **98**, 3307 (1994).
[5] S. Mukamel and J. Jortner, J. Chem. Phys. **61**, 5348 (1974).
[6] T. J. Butenhoff, K. L. Carleton, R. D. van Zee, and C. B. Moore, J. Chem. Phys. **94**, 1947 (1991).
[7] C. Jonah, J. Chem. Phys. **55**, 1915 (1971).
[8] S. Yang and R. Bersohn, J. Chem. Phys. **61**, 4400 (1974).
[9] H.-P. Loock, J. Cao, and C. X. W. Qian, Chem. Phys. Lett. **206**, 422 (1993).
[10] D. H. Mordaunt, M. N. R. Ashfold, and R. N. Dixon, J. Chem. Phys. **104**, 6460 (1996).
[11] S. H. Kable, J. Loison, D. Neyer, P. L. Houston, I. Burak, and R. N. Dixon, J. Phys. Chem. **95**, 8013 (1991).
[12] R. J. Wilson, J. A. Mueller, and P. L. Houston, J. Phys. Chem. **101**, 7593 (1997); J. A. Syage, *ibid.* **105**, 1007 (1996); D. W. Neyer, A. J. R. Heck, and D. W. Chandler, *ibid.* **110**, 3411 (1999).
[13] K.-H. Gericke, M. Lock, R. Fasold, and F. J. Comes, J. Phys. Chem. **96**, 422 (1992).
[14] S. A. Reid and H. Reisler, J. Phys. Chem. **100**, 474 (1996); S. A. Reid, A. Sanov, and H. Reisler, R. Soc. Chem. Faraday Discuss. **102**, 129 (1995).
[15] L. Burnelle, A. M. May, and R. A. Gangi, J. Chem. Phys. **49**, 561 (1968); R. A. Gangi and L. Burnelle, *ibid.* **55**, 851 (1971).
[16] G. Hirsch and R. J. Buenker, Can. J. Chem. **63**, 1542 (1985); G. Hirsch, R. J. Buenker, and C. Petrongolo, Mol. Phys. **70**, 835 (1990).
[17] V. P. Hradil, T. Suzuki, S. A. Hewitt, P. L. Houston, and B. J. Whitaker, J. Chem. Phys. **99**, 4455 (1993); T. Suzuki, V. P. Hradil, S. A. Hewitt, and P. L. Houston, Chem. Phys. Lett. **187**, 257 (1991).
[18] G. E. Bush and K. R. Wilson, J. Chem. Phys. **56**, 3628 (1972); **56**, 3638 (1972).
[19] D. C. Robie, M. Hunter, J. L. Bates, and H. Reisler, Chem. Phys. Lett. **193**, 413 (1992); M. Hunter, S. A. Reid, D. C. Robie, and H. Reisler, J. Chem. Phys. **99**, 1093 (1993).
[20] J. Miyawaki, K. Yamanouchi, and S. Tsuchiya, J. Chem. Phys. **99**, 254 (1993).
[21] G. A. Brucker, S. I. Ionov, Y. Chen, and C. Wittig, Chem. Phys. Lett. **194**, 301 (1992); S. I. Ionov, G. A. Brucker, C. Jaques, Y. Chen, and C. Wittig, J. Chem. Phys. **99**, 3420 (1993); C. Wittig and S. I. Ionov, *ibid.* **100**, 4714 (1994).
[22] H. Gaedtke and J. Troe, Ber. Bunsenges. Phys. Chem. **79**, 184 (1975); M.

Quack and J. Troe, *ibid.* **79**, 469 (1975); H. Gaedtke, H. Hippler, and J. Troe, Chem. Phys. Lett. **16**, 177 (1972).
[23] S. J. Klippenstein and T. Radivoyevitch, J. Chem. Phys. **99**, 3644 (1993).
[24] H. Katagiri and S. Kato, J. Chem. Phys. **99**, 8805 (1993).
[25] M. Kawasaki, H. Sato, A. Fukuroda, T. Kikuchi, S. Kobayashi, and T. Arikawa, J. Chem. Phys. **86**, 4431 (1987).
[26] M. Mons and I. Dimicoli, Chem. Phys. **130**, 307 (1989).
[27] T. J. Butenhoff and E. A. Rohlfing, J. Chem. Phys. **98**, 5460 (1993); **98**, 5469 (1993).
[28] C. Hsieh, Y. Lee, A. Fujii, S. Lee, and K. Liu, Chem. Phys. Lett. **277**, 33 (1997).
[29] J. A. Harrison, X. Yang, M. Rösslein, P. Felder, and J. R. Huber, J. Phys. Chem. **98**, 12260 (1994).
[30] H. Meyer, J. Chem. Phys. **101**, 6686 (1994); *ibid.* **101**, 6697 (1994).
[31] A. Sanov, Th. Droz-Georget, M. Zyrianov, and H. Reisler, J. Chem. Phys. **106**, 7013 (1997).
[32] H. H. Parker and A. Eppink, J. Chem. Phys. **107**, 2357 (1997); Rev. Sci. Instrum. **68**, 3477 (1997).
[33] H. Meyer, J. Chem. Phys. **107**, 7721 (1996).
[34] K. P. Huber and E. Miescher, Helv. Phys. Acta **36**, 257 (1963).
[35] L. D. A. Siebbeles, M. Glass-Maujean, O. S. Vasyutinskii, J. A. Beswick, and O. Roncero, J. Chem. Phys. **100**, 3610 (1994).
[36] K. Blum, *Density Matrix Theory and Application* (Plenum, New York, 1981).
[37] C. H. Greene and R. N. Zare, J. Chem. Phys. **78**, 6741 (1983).
[38] N. Changlong, L. Huan, and J. Pfab, J. Phys. Chem. **97**, 7458 (1993).
[39] R. N. Bracewell, *The Fourier Transform and its Applications* (McGraw-Hill, New York, 1986).
[40] O. Chesnowski and A. Amirav, Chem. Phys. Lett. **109**, 368 (1984).
[41] When the excess energy is a few hundred wave numbers above D_0, the bending frequency in the TS is >20 cm^{-1} (see Refs. 14 and 23).
[42] M. O. Olman and C. D. Hause, J. Mol. Spectrosc. **26**, 241 (1968).
[43] L. B. Harding, H. Stark, J. Troe, and V. G. Ushakov, Phys. Chem. Chem. Phys. **1**, 63 (1999).
[44] S. Yu. Grebenshchikov, C. Beck, H. Flöthman, and R. Schinke, J. Chem. Phys. **111**, 619 (1999).
[45] J. M. Skene, J. C. Drobits, and M. I. Lester, J. Chem. Phys. **85**, 2329 (1986).
[46] P. Pechukas, J. C. Light, and C. Rankin, J. Chem. Phys. **44**, 794 (1966); P. Pechukas and J. C. Light, *ibid.* **42**, 3281 (1965); J. C. Light, Discuss. Faraday Soc. **44**, 14 (1967).
[47] C. Wittig, I. Nadler, H. Reisler, M. Noble, J. Catanzarite, and G. Radhakrishnan, J. Chem. Phys. **83**, 5581 (1985).
[48] The spin-orbit states of NO whose separation is 123 cm^{-1} were suppressed in the simulations.
[49] In the PST/SSE calculations the bending frequency at the TS was taken as 100 cm^{-1}, since the TS is expected to be tighter than a PST-like TS.
[50] F. Santoro and C. Petrongolo, J. Chem. Phys. **110**, 4419 (1999).
[51] I. Nadler, D. Mahgarefteh, H. Reisler, and C. Wittig, J. Chem. Phys. **82**, 3885 (1985).
[52] C. X. W. Qian, A. Ogai, J. Brandon, Y. Y. Bai, and H. Reisler, J. Phys. Chem. **95**, 6763 (1991).
[53] M. Ahmed, D. S. Peterka, A. S. Bracker, O. S. Vasyutinskii, and A. G. Suits, J. Chem. Phys. **110**, 4115 (1999).